Supporting Information:

Complex Stoichiometry-Dependent Reordering of 3,4,9,10-Perylenetetracarboxylic Dianhydride on Ag(111) upon K Intercalation

Christian Zwick❶, Anu Baby❷❸, Marco Gruenewald❶, Elisabeth Verwüster❷, Oliver T. Hofmann❷, Roman Forker❶, Guido Fratesi❹❸, Gian Paolo Brivio❸, Egbert Zojer❷ and Torsten Fritz❶❺*

❶ Institute of Solid State Physics, Friedrich Schiller University Jena, Helmholtzweg 5, 07743 Jena, Germany

❷ Institute of Solid State Physics, NAWI Graz, Graz University of Technology, Petersgasse 16, 8010 Graz, Austria

❸ Department of Materials Science, University of Milano-Bicocca, Via R. Cozzi 55, 20125 Milano, Italy

❹ Dipartimento di Fisica, Università degli Studi di Milano, Via Celoria 16, 20133 Milano, Italy

❺ Osaka University, Graduate School of Science and Institute for Academic Initiatives, Department of Chemistry, 1-1 Machikaneyama, Toyonaka 560-0043, Osaka, Japan

SUPPORTING INFORMATION ON EXPERIMENTS

Degeneration of the $K_{>4}$PTCDA phase.

In the results section of the main manuscript a higher intercalation phase is mentioned which exceeds an effective ratio $x = 4$. The structural properties of this phase are not discussed in detail as it tends to decompose in UHV at room temperature within about an hour (depending on the content of this phase on the surface). This hampers any supporting ST[H]M measurements. Figure S1 (left) shows the corresponding LEED image of the $K_{>4}$PTCDA shortly after preparation. Note that the superimposed simulation of the reciprocal lattice (green) is optimized

1

to give a possible explanation of the $K_{>4}$PTCDA structure by considering all visible diffraction spots. However, the assignment of this structure lacks confirmation by ST[H]M. The mentioned recrystallization of the $K_{>4}$PTCDA phase, which is accompanied by the reformation of the already discussed K_4PTCDA phase, is shown in Figure S1 (center). As can be seen in the red zoom boxes, the intensities of the spots associated with the $K_{>4}$PTCDA and K_4PTCDA phases change continuously. This illustrates the emergence of the K_4PTCDA phase while the $K_{>4}$PTCDA content vanishes. This process results in a sample showing only the K_4PTCDA structure (shown in Figure S1 (right)), which can therefore be assigned as the K intercalated PTCDA phase exhibiting the highest K content that is long-term stable at room temperature.
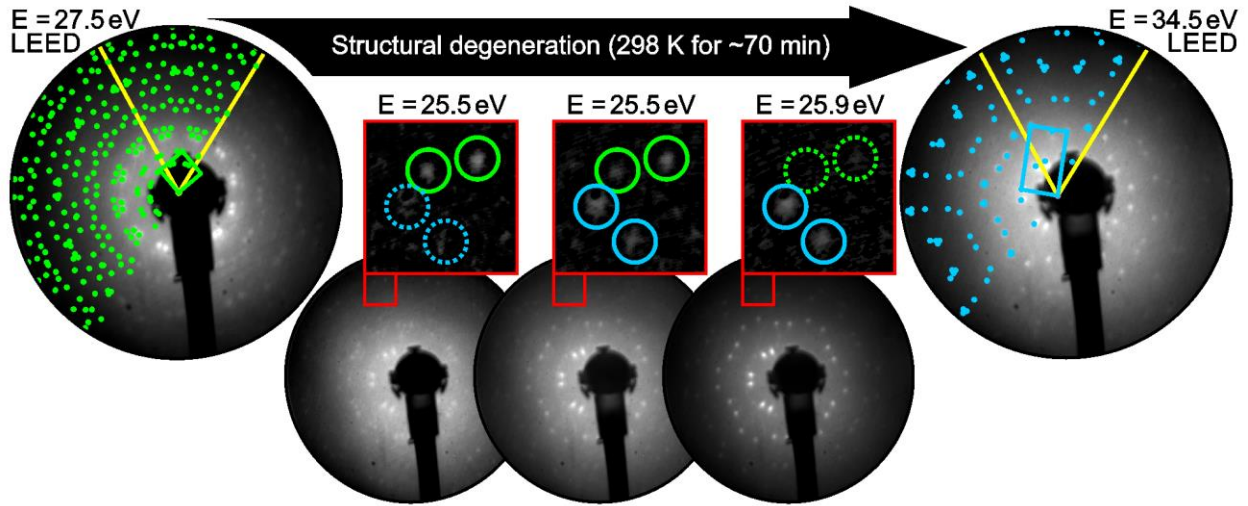

Figure S1. LEED images showing the degeneration of the $K_{>4}$PTCDA phase, accompanied by the renewed formation of the K_4PTCDA structure. The recrystallization occurs at room temperature within approximately 70 min. Samples exhibiting only the $K_{>4}$PTCDA phase (left) and the K_4PTCDA phase (right) are connected by a series of LEED images (center) showing their time-dependent coexistence. The red zoom boxes contain certain contrast-enhanced sections of the LEED images, exhibiting diffraction spots of both structures. The simulation of the reciprocal unit cell of the associated K_xPTCDA structure ($x > 4$ green, $x = 4$ blue) and the silver surface orientation along (01) and (10) (yellow) are superimposed. All possible rotational and mirror domains are considered for the simulation.

Contrast variation in ST[H]M.

In the Methods and Results sections of the manuscript we state that the ST[H]M contrast strongly depends on the tunneling parameters. Figure S2 shows a series of STHM images taken of the K_4PTCDA phase with varying bias voltages while measuring in constant height mode. For the parameters set in Figure S2 (a), the potassium atoms are visible, but not as prominently as the PTCDA molecules. Additionally, not all the K atoms are imaged and the PTCDA exhibits a

different appearance than shown in Figure S2 (b). Changing the parameters to the ones used in Figure S2 (c), the potassium atoms become much more pronounced at the expense of the visibility of the PTCDA molecules. However, an optimal simultaneous visibility of PTCDA and K-related features can be obtained only for parameters close to the ones chosen in Figure S2 (b), where all K atoms are visible, including the mentioned "ghost feature", and also PTCDA displays submolecular resolution.
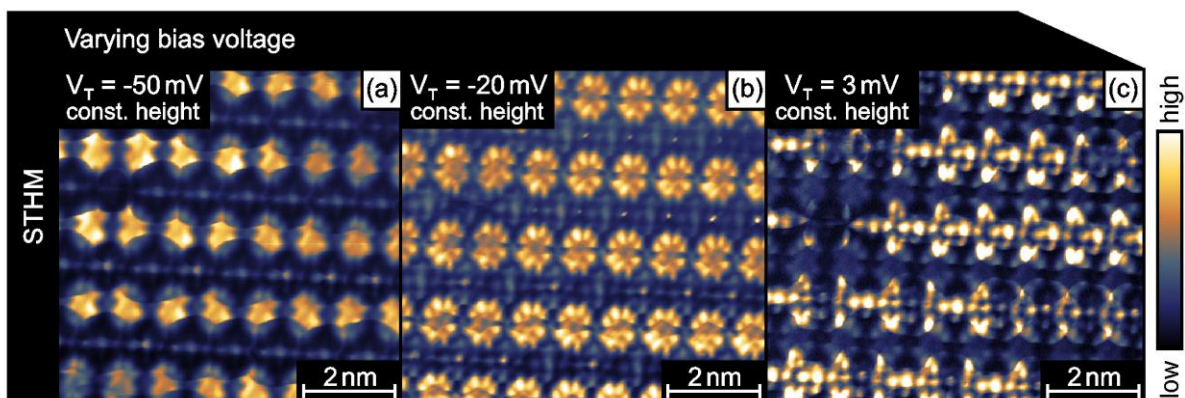

Figure S2. Bias voltage (V_T) dependency of the STHM contrast for images of the K_4PTCDA phase measured in constant height mode. Each image, showing the same sample section, exhibits a significantly different visibility of PTCDA and potassium-related features.

SUPPORTING INFORMATION ON MODELLING

Unit cells used in the simulations of the intercalated interfaces $K_xPTCDA/Ag(111)$.

As described in the Methods section of the main manuscript, to generate a commensurate structure necessary for the periodic boundary simulations, we had to modify the primitive lattice vectors of the substrate surface. Their lengths together with their enclosed angles are summarized in Table S1. To test the impact of those modifications on the electronic structure of the metal, we calculated the resulting work function as well as lattice relaxations. Bottom layers 1, 2 and 3 of the Ag substrate were fixed and the top two layers 4 and 5 were allowed to relax during the optimization calculations. Δz^{surf} indicates the height difference between the 5th and 4th layers after relaxation and Δz^{bulk} indicates the height difference between the 1st and 2nd layers. The quantity in the last column of Table S1 shows how much the top two layers have relaxed with respect to the bottom three layers (which essentially represent the bulk). The work function is in all cases within $0.04\,eV$ from the value obtained for a lattice constant optimized using PBE, and the lattice relaxation is in good agreement with the experiment. For calculating K_3PTCDA and K_5PTCDA on Ag(111) the same unit cells as for K_4PTCDA were used (with an appropriately reduced or increased number of K atoms, respectively).

Table S1. The rounded epitaxy matrix M′, resulting commensurate Ag substrate unit cell vectors $\vec{s}_1$ and $\vec{s}_2$ as well as the angle between them $\gamma = \sphericalangle(\vec{s}_1, \vec{s}_2)$, substrate work function, surface interlayer spacing Δz^{surf} and the comparison to the bulk interlayer spacing Δz^{bulk}. All values are given for bare Ag(111) substrates for the pristine surface with optimized lattice constants (PBE) and for the modified surfaces later used to accomodate commensurate K_2PTCDA and K_4PTCDA structures. Experimental values are given for comparison.

	Epitaxy matrix M'	$\lvert\vec{s}_1\rvert, \lvert\vec{s}_2\rvert$ [Å]	γ [°]	Work function (eV)	Δz^{surf} [Å]	$\Delta z^{surf}\text{-}\Delta z^{bulk}$ [Å]
K_2PTCDA	$\begin{bmatrix} 3 & 0 \\ 1 & 6 \end{bmatrix}$	2.9718, 2.8690	118.03	4.46	2.36	-0.06
K_4PTCDA	$\begin{bmatrix} 7 & 6 \\ 1 & 7 \end{bmatrix}$	2.9799, 2.9173	120.96	4.49	2.39	-0.05
PBE	-	2.9460, 2.9460	120.00	4.46 (4.45 [1])	2.375	-0.03
Experiment	-	-	-	4.46, [2] 4.5, [3] 4.74 [4]	-	-0.06 [5]

At first glance the relation between the epitaxy matrix for K_4PTCDA listed in Table S1 and that in Table 1 in the main manuscript is not obvious. Still they are directly related: The rounded version of the epitaxy matrix shown in the manuscript required for constructing a commensurate superstructure is $\begin{pmatrix} 3.5 & 3 \\ -2.5 & 4 \end{pmatrix}$. Subsequently, a 2×2 supercell is created from that matrix. This results in a structure commensurate with the Ag(111) surface, as shown by the blue lines in Figure S3. The disadvantage of this structure is that it contains 4 PTCDA molecules per unit cell, which makes it extremely costly to simulate. This led us to pick an alternative commensurate unit cell depicted by the green lines in Figure S3, corresponding to an epitaxy matrix $\begin{pmatrix} 7 & 6 \\ 1 & 7 \end{pmatrix}$, which contains only two molecules.
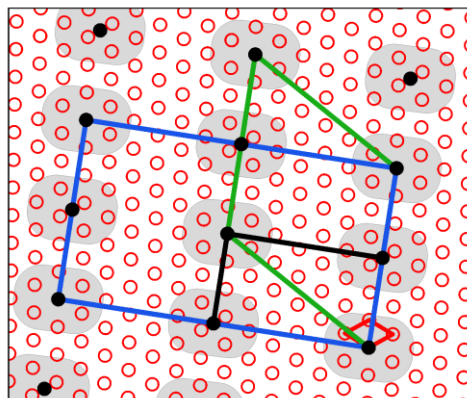
Figure S3. Possible supercells that can be used as commensurate adsorbate structures to approximately describe the K_4PTCDA layer on Ag(111). Red dots and lines mark the Ag(111) substrate lattice and unit cell, while black ones refer to the adsorbate layer according to the rounded epitaxy matrix $\begin{pmatrix} 3.5 & 3 \\ -2.5 & 4 \end{pmatrix}$ (schematic PTCDA molecules are shaded grey to help guide the eye). The commensurate super cells corresponding to the epitaxy matrices $\begin{pmatrix} 7 & 6 \\ -5 & 8 \end{pmatrix}$ and $\begin{pmatrix} 7 & 6 \\ 1 & 7 \end{pmatrix}$ are shown in blue and green, respectively.

Optimized structures obtained for K_2PTCDA, K_3PTCDA, K_4PTCDA, and K_5PTCDA, are shown in Figure S4, Figure S5, Figure S6, and Figure S7. The simulated STM images for K_3PTCDA and K_5PTCDA are given in Figure S8 and Figure S9, respectively.
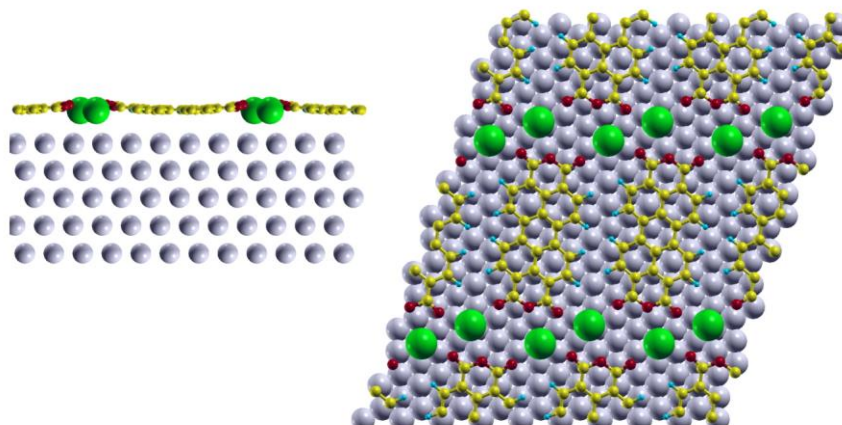

Figure S4. Side (left) and top view (right) of the optimized structure obtained for K_2PTCDA on Ag(111).
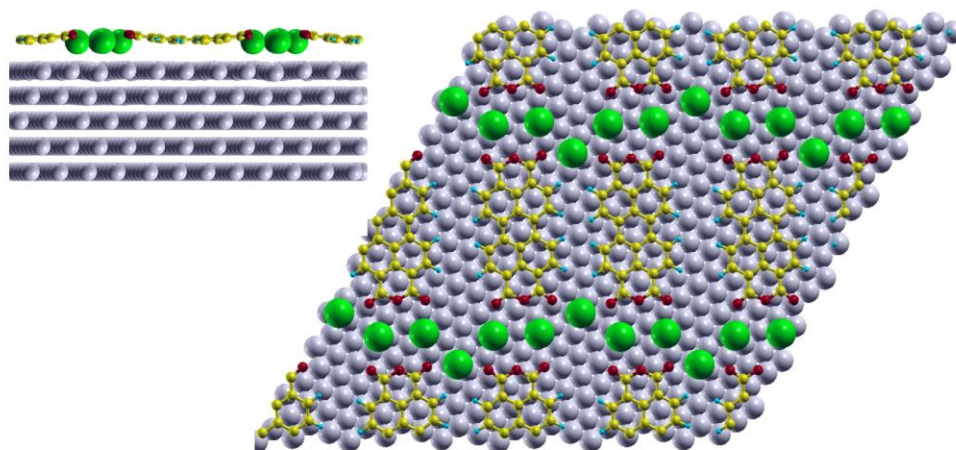
Figure S5. Side (left) and top view (right) of the optimized structure obtained for K_3PTCDA on Ag(111).
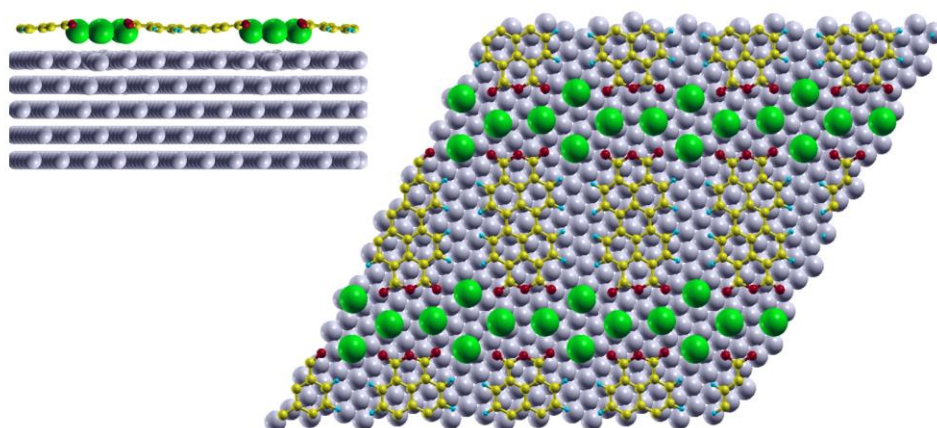

Figure S6. Side (left) and top view (right) of the optimized structure obtained for K_4PTCDA on Ag(111).
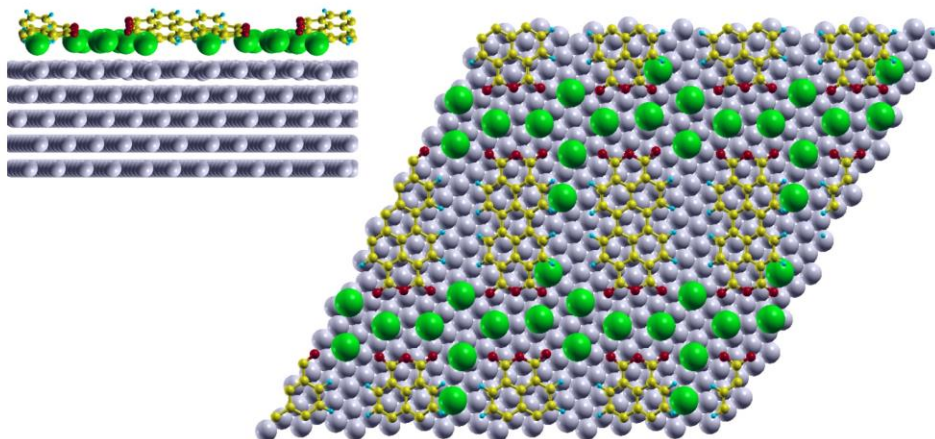
Figure S7. Side (left) and top view (right) of the optimized structure obtained for K_5PTCDA on Ag(111).
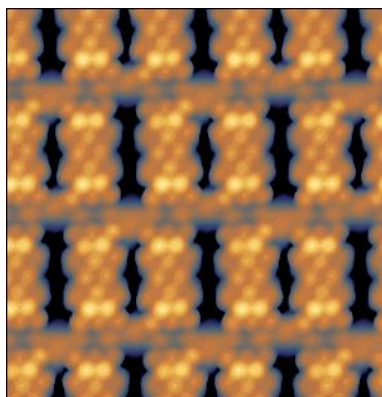

Figure S8. Simulated constant current STM image obtained for K_3PTCDA at $V_T = 0.6$ V and $\rho_{iso} = 0.3$ meÅ^{-3}.
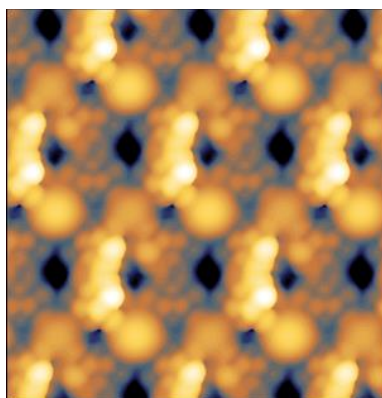

Figure S9. Simulated constant current STM image obtained for K_5PTCDA at $V_T = 0.8$ V and $\rho_{iso} = 0.3$ meÅ^{-3}.

Layer formation energies.

The layer formation energies per molecule of the different phases of K_xPTCDA on Ag(111) were calculated using the following equation:

$$E_{layer}(K_xPTCDA) = N^{-1} \cdot \left(E(K_xPTCDA) - E(Ag(111)) - N \cdot E(PTCDA) - M \cdot E(K) \right) \qquad (1)$$

The various energies refer to the energies per unit cell and energy of individual atoms or molecules, respectively. N is the number of PTCDA molecules in the unit cell and M that of K atoms. The geometries of the combined systems and of the fundamental constituents were fully optimized; the geometries of intermediate stage situations (like the free-standing K_2PTCDA layer) were left as determined for the respective combined system. The calculated layer formation energies per molecule for the distinct K_xPTCDA phases are listed in Table S2.

Table S2. Layer formation energy per molecule (or atom in the case of pristine K) E_{layer} for the distinct phases of K_xPTCDA, pristine PTCDA, and pristine potassium on Ag(111). All quantities used for the calculation of E_{layer} according to equation (1) are listed.

Ag(111) lattice parameters as in:	E(K_xPTCDA) (eV)	E(Ag(111)) (eV)	N	E(PTCDA) (eV)	M	E(K) (eV)	E_{layer}(eV)
K/Ag(111)	-118.62	-116.00	0	-287.72	1	-0.12	-2.49
PTCDA/ Ag(111)	-1009.14	-425.40	2	-287.72	0	-0.12	-4.01
K_2PTCDA	-531.32	-231.74	1	-287.72	2	-0.12	-11.61
K_3PTCDA	-1160.50	-554.95	2	-287.72	6	-0.12	-14.69
K_4PTCDA	-1168.60	-554.95	2	-287.72	8	-0.12	-18.61
K_5PTCDA	-1174.32	-554.95	2	-287.72	10	-0.12	-21.35

Electronic properties of the adsorbate layer.

In the calculated density of states we see that the LUMO is filled to a significant extent for PTCDA on Ag(111), an effect that is well documented in experiments[6,7] and in simulations.[1] The LUMO-derived band shifts to higher binding energies upon K deposition in K_2PTCDA and K_4PTCDA on Ag(111). Further insight into the involved charge-transfer processes can be gained from an analysis of the molecular and atomic charges (of PTCDA and K respectively) in the involved species. To that aim we performed a Bader Charge Analysis[8] based on the charge densities calculated with VASP. This analysis reveals that the negative charge on each PTCDA molecule increases upon potassium deposition, *i.e.*, the charge per molecule increases from 1.1 electrons for PTCDA/Ag(111) *via* 1.7 electrons per molecule for K_2PTCDA/Ag(111) to 1.9 electrons per molecule in K_4PTCDA/Ag(111). Interestingly, while for PTCDA/Ag(111) the electrons transferred to PTCDA obviously originate from the Ag substrate, the net charges on the Ag atoms are apparently hardly affected by the interaction with the adsorbate in K_2PTCDA/Ag(111), *i.e.*, there the negative net charge on PTCDA directly correlates with an approximately equally large positive charge on the K atoms and the Bader charge on the Ag substrate is negligibly small. In the case of K_4PTCDA/Ag(111) the decrease of the electron density on the K atoms additionally gives rise to an increased electron density in the Ag substrate (1.1 electrons per K_4 cluster in the K_4PTCDA phase; *i.e.*, the K atoms transfer electrons to the PTCDA molecules and to the Ag substrate, which results in a net charge of every K atom of ~ -0.8 electrons).

Technical details regarding the Bader charge analysis: We used version 0.95 of the Bader Charge Analysis code released by the Henkelman group.[9-12] For producing reliable charge densities for the analysis, we reran the VASP calculations applying the so-called aedens module to write out also the core-densities from the PAW calculations and used accurate settings especially for enforcing a more dense mesh in the FFT procedure.

Frontier states of a charged K_4 cluster.

In order to better understand the nature of the dominant feature between the K atoms in the ST(H)M experiments on the K_4PTCDA system, we calculated the electronic properties of a K_4 cluster arranging the atoms at exactly the same positions at which we find them when optimizing the full K_4PTCDA/Ag(111) interface. The respective lowest unoccupied state of the four-fold positively charged cluster (*i.e.*, a cluster in which each K atom has lost an electron, which according to the above mentioned Bader charge analysis very well represents the situation of K_4 at the interface) is shown in Figure S10.
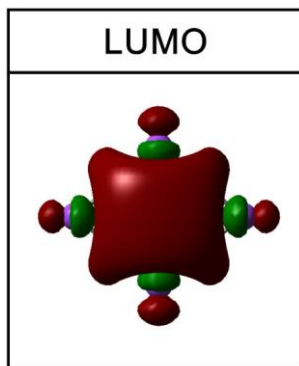
Figure S10. Lowest unoccupied molecular orbital (LUMO) of a K_4^{4+} four-fold positively charged cluster (K is represented by purple balls).

One clearly sees that the lowest unoccupied molecular orbital (LUMO) for K_4^{4+} originates from a bonding, in phase superposition of potassium hybrid orbitals, which is characterized by a massive wave function amplitude between the K atoms strongly reminiscent of the feature seen in STM. In passing, we note that an equivalent orbital is found as the HOMO-1 in the neutral cluster showing that the occurrence of that orbital is not an artifact of the calculations on the highly charged cluster. Moreover, also when using a hybrid-functional (here B3LYP) the said orbital is obtained as the LUMO of K_4^{4+}.

Details of the computation: The calculations on the K_4 clusters were performed using Gaussian09[13] and employing the PBE[14] functional in conjunction with the 6-311G(d,p) basis set.[15]

Critical assessment of the Tersoff-Hamann approach; s- vs. p-type character of the tip wave function.

Martínez *et al.*[16] have suggested that one of the origins of the improved resolution for H-sensitized tips is the increased p-type character of the tip wave function, which raises the question to what extent applying the Tersoff-Hamann approach is appropriate (as it assumes an s-type tip). This question shall be addressed in the following.

First it should be stressed that assumptions made in the Tersoff-Hamann approach should not be confused with properties of actual electronic states at the tip. As already described in the original paper by Tersoff and Hamann, "the s-wave treatment here is not intended as an accurate description of a real tip, but rather as a useful way of parameterizing the effect of finite tip size".[17] This approximation is rather done, as the tunneling matrix element becomes particularly simple, when treating the tip "as a locally spherical potential well where it approaches nearest the surface" and then considering only the solution with an s-type angular momentum.[17] Another reason why a strictly atomistic interpretation of the s-type tip wave

function is not useful here is the averaging procedure we applied (for details see Methods section).

Still, applying the Tersoff-Hamann approach is useful for obtaining qualitative and here also semi-quantitative insight. This is because at a reduced tip-to-sample distance it can be viewed as the simplest model of a tip providing atomic resolution. This approximation, of course, does not capture the $\partial\Psi/\partial z$ "character" of the tunneling matrix element for a p_z-type wave function, but as shown by Chen for an Al(111) surface, the lateral resolution of a d_{z^2} tip becomes comparable to that of an s-wave model at a significantly reduced (*i.e.*, smaller than experimentally possible) tip-to-sample distance.[18] Moreover, Olsson *et al.*[19] have shown for chemisorbed O_2 on Ag(110) that simulating STM assuming a p_z-type tip yields essentially identical constant-current STM profiles as when considering an s-type tip at a distance reduced by 1 Å. As far as p_x- and p_y-type tips are concerned, these would indeed create significant differences in the shape of the STM images.[20] Such contrast can, for example, be obtained when scanning with a CO functionalized tip.[20] It is *a priori* not clear, where such states would originate from in an STHM experiment, in particular, as Martínez *et al.* have shown that the H_2 molecules dissociate on the Au tip; similar results were apparently obtained for tungsten tips.[16] Moreover, we do not see any indications for p_x/p_y character in the experimental data.

Another reason, why resorting to a Tersoff-Hamann approach at effectively reduced distances is useful is that merely accounting for the $\partial\Psi/\partial z$ "character" of the tunneling matrix element very likely would not yield a fully quantitative description either. In STHM one potentially encounters a very complex situation in which the sensitizing molecule directly couples with the molecules that are measured; *i.e.*, the electronic structure of the tip and the sample is altered by the measurement process. For example, Martínez *et al.*[16] describe significant shifts in the positions of the PTCDA electronic states relative to E_F induced by the tip (in particular, the H atom at the tip) in the STHM experiment. Alternatively, the hydrogen between tip and sample acts as a transducer, transforming short ranged Pauli repulsion induced forces into a change in tunneling conductance with a therefore strong dependence on local properties.[21] This is in agreement with the experiments, where a drastic change of contrast is achieved, once the hydrogen is trapped successfully in the tunneling junction (see Methods section). A comprehensive study along these lines would require testing a tip against a well-studied reference surface,[22] which is clearly beyond the scope of the present work.

REFERENCES

[1]   Romaner, L.; Nabok, D.; Puschnig, P.; Zojer, E.; Ambrosch-Draxl, C. Theoretical study of PTCDA adsorbed on the coinage metal surfaces, Ag(111), Au(111) and Cu(111). *New J. Phys.* **2009**, *11*, 053010.

[2]   Chelvayohan, M.; Mee, C. H. B. Work function measurements on (110), (100) and (111) surfaces of silver. *J. Phys. C: Solid State Phys.* **1982**, *15*, 2305.

[3]   Rangger, G. M.; Hofmann, O. T.; Romaner, L.; Heimel, G.; Bröker, B.; Blum, R.-P.; Johnson, R. L.; Koch, N.; Zojer, E. F4TCNQ on Cu, Ag, and Au as prototypical example for a strong organic acceptor on coinage metals. *Phys. Rev. B* **2009**, *79*, 165306.

[4]   Michaelson, H. B. The work function of the elements and its periodicity. *J. Appl. Phys.* **1977**, *48*, 4729–4733.

[5]   Statiris, P.; Lu, H. C.; Gustafsson, T. Temperature dependent sign reversal of the surface contraction of Ag(111). *Phys. Rev. Lett.* **1994**, *72*, 3574–3577.

[6]   Hauschild, A.; Karki, K.; Cowie, B. C. C.; Rohlfing, M.; Tautz, F. S.; Sokolowski, M. Molecular Distortions and Chemical Bonding of a Large π-Conjugated Molecule on a Metal Surface. *Phys. Rev. Lett.* **2005**, *94*, 036106.

[7]   Duhm, S.; Gerlach, A.; Salzmann, I.; Bröker, B.; Johnson, R. L.; Schreiber, F.; Koch, N. PTCDA on Au(111), Ag(111) and Cu(111): Correlation of interface charge transfer to bonding distance. *Org. Electron.* **2008**, *9*, 111–118.

[8]   Bader, R. F. W. *Atoms in Molecules: A Quantum Theory*; Oxford University Press, New York, 1990.

[9]   Henkelman, G.; Arnaldsson, A.; Jónsson, H. A fast and robust algorithm for Bader decomposition of charge density. *Comput. Mater. Sci.* **2006**, *36*, 354–360.

[10] Sanville, E.; Kenny, S. D.; Smith, R.; Henkelman, G. Improved grid-based algorithm for Bader charge allocation. *J. Comput. Chem.* **2007**, *28*, 899–908.

[11] Tang, W.; Sanville, E.; Henkelman, G. A grid-based Bader analysis algorithm without lattice bias. *J. Phys.: Condens. Matter* **2009**, *21*, 084204.

[12] Yu, M.; Trinkle, D. R. Accurate and efficient algorithm for Bader charge integration. *J. Chem. Phys.* **2011**, *134*, 064111.

[13] Frisch, M. J. et al. Gaussian09 Revision C.01. Gaussian Inc. Wallingford CT 2009.

[14] Perdew, J. P.; Burke, K.; Ernzerhof, M. Generalized Gradient Approximation Made Simple. *Phys. Rev. Lett.* **1996**, *77*, 3865–3868.

[15] Blaudeau, J.-P.; McGrath, M. P.; Curtiss, L. A.; Radom, L. Extension of Gaussian-2 (G2) theory to molecules containing third-row atoms K and Ca. *J. Chem. Phys.* **1997**, *107*, 5016.

[16] Martínez, J. I.; Abad, E.; González, C.; Flores, F.; Ortega, J. Improvement of Scanning Tunneling Microscopy Resolution with H-Sensitized Tips. *Phys. Rev. Lett.* **2012**, *108*, 246102.

[17] Tersoff, J.; Hamann, D. R. Theory of the scanning tunneling microscope. *Phys. Rev. B* **1985**, *31*, 805–813.

[18] Chen, C. J. Origin of atomic resolution on metal surfaces in scanning tunneling microscopy. *Phys. Rev. Lett.* **1990**, *65*, 448–451.

[19] Olsson, F. E.; Lorente, N.; M., P. STM images of molecularly and atomically chemisorbed oxygen on silver. *Surf. Sci.* **2003**, *522*, L27 – L35.

[20] Gross, L.; Moll, N.; Mohn, F.; Curioni, A.; Meyer, G.; Hanke, F.; Persson, M. High-Resolution Molecular Orbital Imaging Using a *p*-Wave STM Tip. *Phys. Rev. Lett.* **2011**, *107*, 086101.

[21] Weiss, C.; Wagner, C.; Kleimann, C.; Rohlfing, M.; Tautz, F. S.; Temirov, R. Imaging Pauli Repulsion in Scanning Tunneling Microscopy. *Phys. Rev. Lett.* **2010**, *105*, 086103.

[22] Donati, F.; Fratesi, G.; Ning, L.; Brambilla, A.; Trioni, M. I.; Li Bassi, A.; Casari, C. S.; Passoni, M. Electronic and magnetic properties of bulk Cr tips for scanning tunneling spectroscopy. *Phys. Rev. B* **2013**, *87*, 235431.